iScience

CellPress
OPEN ACCESS

Article

Alcohol imination catalyzed by carbon nanostructures synthesized by C(sp^2)-C(sp^3) free radical coupling

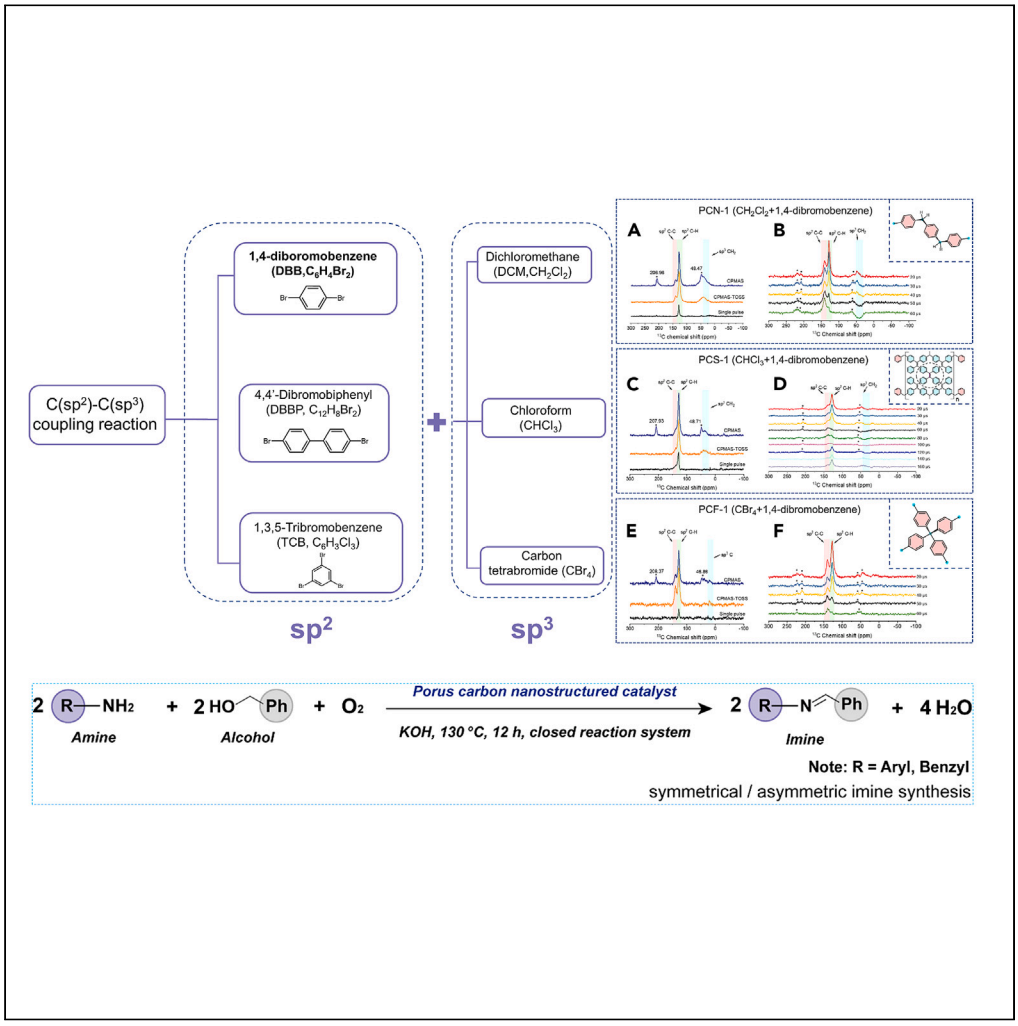

Cheng Wang, Zirui Qiao, Yulan Tian, Haijun Yang, Huaqiang Cao, Anthony K. Cheetham

hqcao@mail.tsinghua.edu.cn (H.C.)
akc30@cam.ac.uk (A.K.C.)

Highlights

A free-radical coupling approach to generate high-spin carbon nanostructures

The carbon nanostructures can be identified by solid-state NMR

The imidization reactions catalyzed by carbon nanostructures

Wang et al., iScience 26, 106659
May 19, 2023
https://doi.org/10.1016/j.isci.2023.106659

iScience

CellPress
OPEN ACCESS

Article

Alcohol imination catalyzed by carbon nanostructures synthesized by C(sp^2)-C(sp^3) free radical coupling

Cheng Wang,[1,3] Zirui Qiao,[1,3] Yulan Tian,[1,3] Haijun Yang,[1] Huaqiang Cao,[1,4,*] and Anthony K. Cheetham[2,*]

SUMMARY

Imines are important intermediates for synthesizing various fine chemicals, with the disadvantage of requiring the use of expensive metal-containing catalysts. We report that the dehydrogenative cross-coupling of phenylmethanol and benzylamine (or aniline) directly forms the corresponding imine with a yield of up to 98%, and water as the sole by-product, in the presence of a stoichiometric base, using carbon nanostructures as the "green" metal-free carbon catalysts with high spin concentrations, which is synthesized by C(sp^2)-C(sp^3) free radical coupling reactions. The catalytic mechanism is attributed to the unpaired electrons of carbon catalysts to reduce O_2 to $O_2^{\cdot-}$, which triggers the oxidative coupling reaction to form imines, whereas the holes in the carbon catalysts receive electrons from the amine to restore the spin states. This is supported by density functional theory calculations. This work will open up an avenue for synthesizing carbon catalysts and offer great potential for industrial applications.

INTRODUCTION

Imines, with C=N functional groups, also called "Schiff bases",[1] are significant intermediates in the synthesis of fine chemicals,[2] pharmaceuticals,[3] biological actives, such as anti-inflammatories, anti-cancer drugs, and antimicrobials,[4] and molecular motors.[5,6] In addition, the imine's C=N groups, acting as electrophiles toward carbon nucleophiles in a reaction that leads to the formation of C-C bonds, are very important functional groups in organic chemistry.[7,8] Different approaches for synthesizing imines have led to significant developments, including condensation of amines with carbonyl compounds,[9] self-condensation of primary amines with oxidants,[10] oxidation of secondary amines,[11] and coupling of amines with primary alcohols in the presence of a catalyst.[12] However, with few exceptions,[13] most of the synthesis methods for making imines require expensive metal-containing catalysts.[14] It is well known that the natural resources of precious metals are limited.[15] The ideal catalyst, therefore, should not contain precious metals.[16]

Innovative materials as alternatives to the above-mentioned metal catalysts have been designed using the bottom-up approaches. They include organocatalysts,[15] such as covalent triazine frameworks (CTFs) for the selective oxidation of alcohols to the corresponding aldehyde/ketone,[17] ketone-amine condensations by 4-methylanthranilic acid to α-amino enone with 37% yield,[18] alcohol amination with an amine to form secondary amine by carbon-based catalysts,[19] and selective oxidation of N-heterocycles compounds to quinoline and indole catalyzed by polymaleimide derivatives.[20]

Since the first report of spin catalysis in 1994,[21] it has been found that many spin carriers can serve as spin catalysts, which makes it possible to overcome spin conservation rules in basic chemical reactions, thus increasing the possibility of chemical reaction success.[22–24] There are two important mechanisms of spin catalysis: (1) Exchange (nonmagnetic) interactions of electron spins, and (2) dipole-dipole interactions of electron spins through their magnetic dipoles.[23] Carbon, being abundantly available, is a very promising candidate for constructing carbon-based materials that can act as metal-free catalysts with different electronic states and molecular structures. Stable carbon-centered neutral radicals, including open-shell graphene as a gigantic π-conjugated aromatic hydrocarbon[25–27] that has the spin states of a multielectron system,[28] can function as spin catalysts by allowing spin-flip processes during a reaction.[24] Here, we report the use of a free radical C(sp^2)-C(sp^3) coupling reaction to synthesize two-dimensional (2D) carbon nanosheets and three-dimensional (3D) carbon organic framework (COF) nanostructures with high electron spin

[1]Department of Chemistry, Tsinghua University, Beijing 100084, China

[2]Materials Research Laboratory, University of California, Santa Barbara, Santa Barbara, CA 93106, USA

[3]These authors contributed equally

[4]Lead contact

*Correspondence: hqcao@mail.tsinghua.edu.cn (H.C.), akc30@cam.ac.uk (A.K.C.)

https://doi.org/10.1016/j.isci.2023.106659

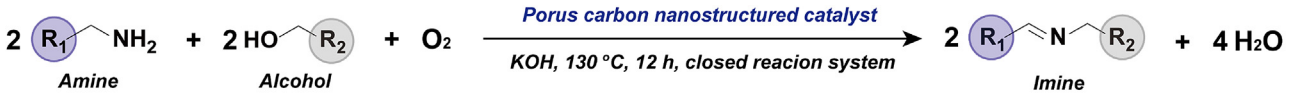

Figure 1. Catalyzed dehydrogenative coupling of benzyl alcohol and benzylamine (or aniline)

densities. These materials can be applied as spin catalysts in a direct imine synthesis via aerobic oxidative coupling of an alcohol (benzyl alcohol) and an amine (benzylamine or aniline). The reaction proceeds at 130 °C for 12 h in a closed reaction system, with the liberation of H_2O as the only by-product, and without the formation of the corresponding amides or amines.

RESULTS AND DISCUSSION

The synthetic strategy for the porous carbon nanostructures

A general bottom-up approach was designed to synthesize nanostructured carbon catalysts (Figures 1 and 2) with high spin concentrations on the order of 10^{20} spin·g^{-1} (electron spin resonance, ESR, spectra, Table S1). The synthesis proceeded via a C(sp^2)-C(sp^3) free-radical coupling reaction using small organic molecules, i.e. carbon tetrabromide (CBr_4), chloroform ($CHCl_3$), or dichloromethane (CH_2Cl_2) as the sp^3-carbon monomer, together with 1,4-dibromobenzene ($C_6H_4Br_2$), 4,4′-dibromobiphenyl ($C_{12}H_8Br_2$) or 1,3,5-tribromobenzene ($C_6H_3Br_3$), as the sp^2-carbon monomers. These were reacted with sodium metal under solvothermal conditions to form three types of porous carbon nanostructures (Brunauer-Emmett-Teller, BET data, Table S2): (1) A 3D porous carbon chain network (3D-PCN) (Figures 2A and 2i-iii) with crosslinked network features, (2) 2D porous carbon sheets (2D-PCS) (Figures 2B and 2i-iii) with nanosized pores that are distributed throughout the sheets, as observed by atomic force microscopy (AFM) (top right corner of Figures 2B–2i) (the pores can also be observed clearly in our transmission electron microscopy, TEM images and optical images, OM) (Figures 2, S1, and S2), and (3) 3D porous carbon frameworks (3D-PCF) (Figures 2C and 2i-iii). Detailed experimental procedures are provided in the supplemental information. It should be noted that both trichloromethane ($CHCl_3$) and tribromethane ($CHBr_3$) are gases, so the reactions between CHX_3 (X = Cl, or Br) and Na were excluded from this study.

Structural characterization

Detailed structure information of the three types of as-synthesized carbon nanostructures was obtained for the selected samples of the PCN-1 (Figures 2A–2i), the PCS-1 (Figures 2B–2i), and the PCF-1 (Figures 2C–2i), respectively. X-ray photoelectron spectroscopy (XPS) data (Figure 3A) show that the products contain C and O on the surface, but do not contain the halogen elements (Cl or Br) derived from the starting reagents, indicating that the halogens are completely removed from the reaction products after the coupling reaction. The C1s peak can be deconvoluted into five subpeaks, such as C=C at ~284.7 eV (83.5 at%), and C-C at ~285.8 eV (1.8 at%), as well as C-O, C=O, and O-C=O for the PCS-1 (Figure S4 and Table S4). Similar results are shown in Figure S3 and Table S3 for the PCN-1, and Figure S5 and Table S5 for the PCF-1, respectively. The observation of inhomogeneous aggregates is attributed to the coupling between dangling bonds, and reactions between the oxygen-containing groups, such as hydroperoxides ROOH, benzyloxy radicals, hydroxyl-containing compounds, and benzyl radicals, carboxyl groups, etc., which are generated by O_2 and/or CO_2 in the reaction system as inhibitors in the radical coupling reaction.[29,30] X-ray diffraction (XRD) measurements were carried out to explore the presence of any crystallinity (Figure 3B). The patterns contain a broad diffraction peak in the 2θ range 18–24° and a hump in the range 40–50°, indicating that the three samples are amorphous in nature.[31] Sodium halide by-products can also be identified by XRD (Figures S7A–S7C), which further demonstrates that dehalogenation occurred during the synthesis procedure. The Raman spectra of the PCN-1, PCS-1, and PCF-1 show two peaks: a stronger peak at ~1589.0 cm^{-1} called the G-band, from the in-plane vibration of the sp^2 carbon atoms, and a weaker peak at ~1356.9 cm^{-1} called the D-band, from the out-of-plane vibration of the carbon atoms; the latter is forbidden in perfect graphite and only becomes active in the presence of disorder.[32] Thus, the Raman data also indicate that defects and disorders are present in the as-synthesized carbon materials (Figure 3C). The presence of aromatic rings in the as-synthesized samples is also demonstrated by Fourier transform infrared spectroscopy (FTIR, Figure 3D), where the weak aromatic C-H stretching vibration near 3030 cm^{-1}, two or three C=C stretching vibrations in the region of 1600-1500 cm^{-1} that is usually observed in most six-membered

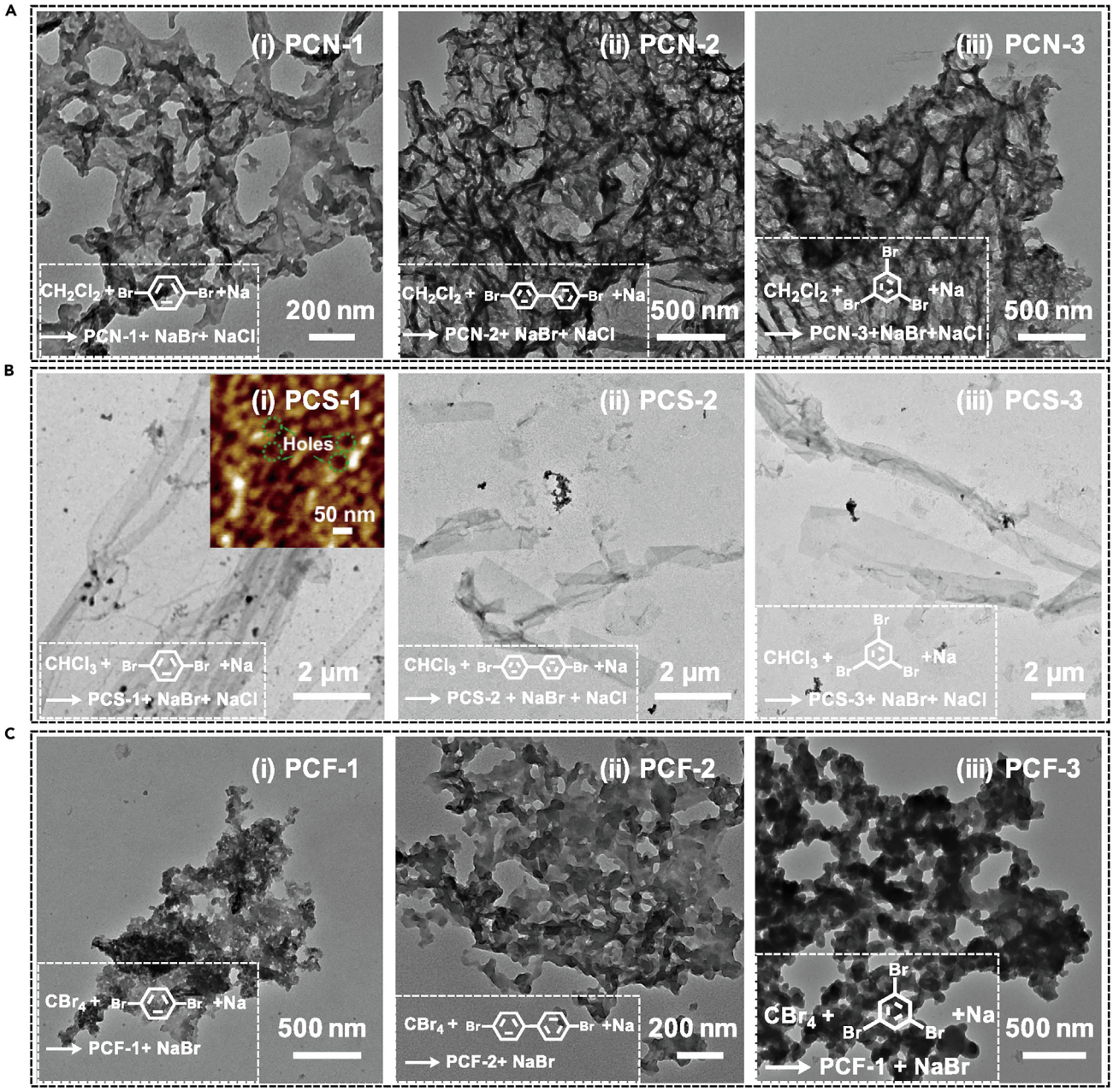

Figure 2. TEM images of the carbon nanostructures, where the bottom left corner of each image presents the corresponding reaction equation

(A) (i) PCN-1, (ii) PCN-2, and (iii) PCN-3.

(B) (i) PCS-1 (the top right corner inset refers to an AFM image that represents the porous structure), (ii) PCS-2, and (iii) PCS-3.

(C) (i) PCF-1, (ii) PCF-2, and (iii) PCF-3.

aromatic ring systems, and a group of bands below 900 cm^{-1} that can be attributed to the our-of-plane C-H bending vibration, can be observed, whereas bands in the range of 1225-950 cm^{-1} seldom provide structural information.[33] Electron spin resonance (ESR) spectra reveal that the *g*-values of the PCN-1, PSCS-1, and PCF-1 are 2.0028, 2.0027, and 2.0026 (all less than 2.0030), respectively (Figure 3E and Table S1), indicating that stable carbon-centered free radicals (namely dangling bonds) are present in the as-synthesized carbon nanostructures.[34] The samples contain high electron spin densities, in the range 2.6–6.3 × 10^{20} spins·g^{-1} (Table S1), which is four orders of magnitude above that of graphene oxide (GO) (8.2× 10^{16} spins·g^{-1})[35] and is ascribed to the emergence of carbon vacancies in the form of stable radicals because

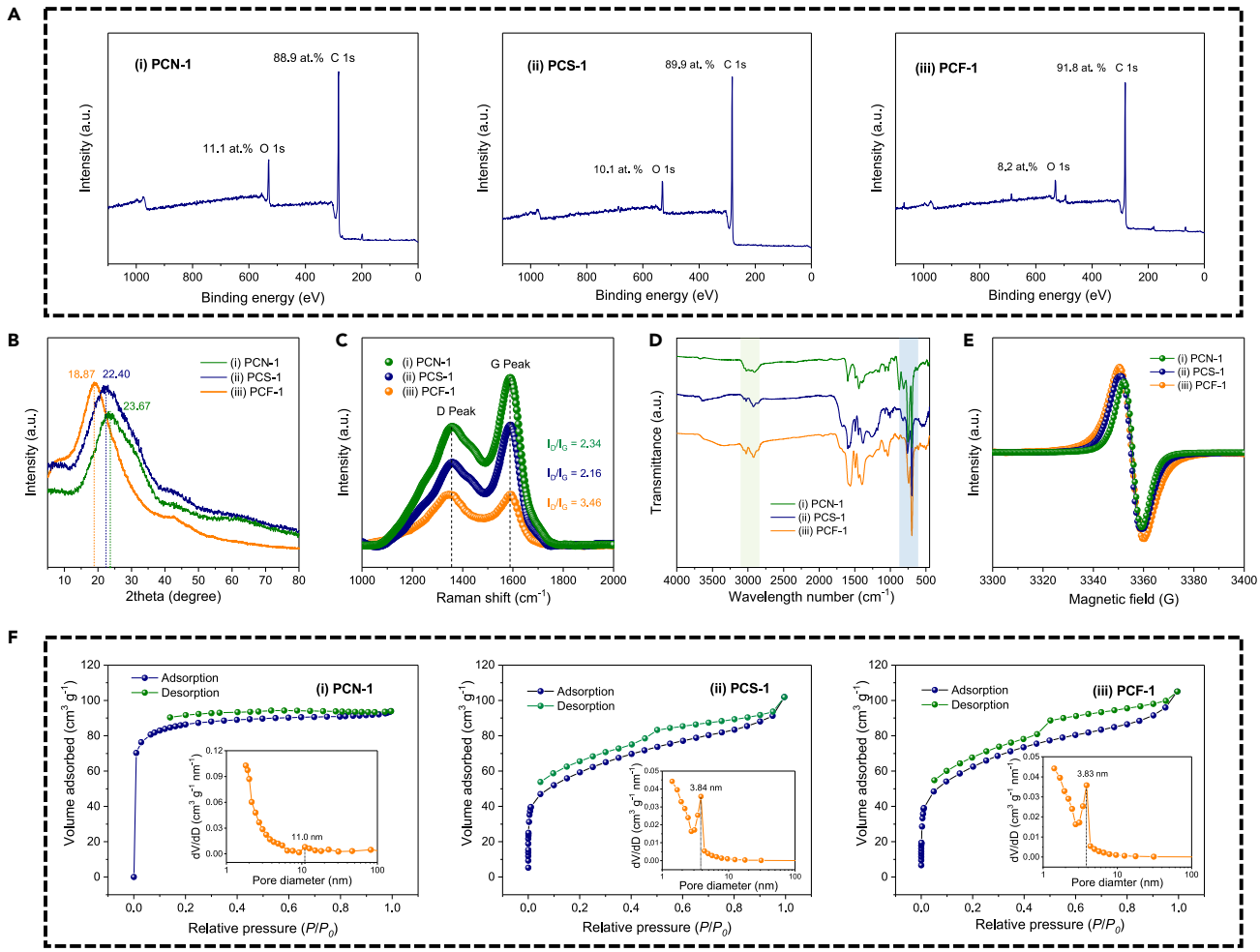

Figure 3. Physical characterizations of the samples

(A) XPS patterns.

(B) XRD patterns.

(C) Raman spectra.

(D) FTIR spectra.

(E) ESR spectra.

(F) BET surface areas, and pore size distributions. Note: (i) PCN-1, (ii) PCS-1, and (iii) PCF-1.

of the different synthesis method.[36] The N_2 adsorption isotherms of these three samples show representative Type-IV curves with typical H3-type hysteresis loops (Figure 3F (i)-(iii) and Table S2). This confirms that the as-synthesized carbon nanostructures have high surface areas and porous characteristics,[37] with well-defined mesopores, based on the IUPAC definition, with sizes of 11.0 nm, 3.84 nm, and 3.83 nm, respectively (Insets, in the bottom right corner of Figure 3F (i)-(iii)). The highly porous structures of PCN-1, PSCS-1, and PCF-1 can provide large surface areas for good accessibility to the activity sites[38]; this will be discussed further below in the context of the catalytic reactions. The C/H atom ratios, based on element analysis (Table S6), for the PCN-1, PCS-1, and PCF-1 are approximately 1.36, 1.32, and 1.41, respectively. These data are close to their corresponding theoretical values of C/H atom ratios. The sp^2/sp^3 carbon ratios for the PCN-1, PCS-1, and PCF-1, based on XPS data (Tables S3–S5) are 6.3, 46.4, and 11.7, respectively, which are close to the results from X-ray absorption near edge structure (XANES) spectra (Figure S6, Table S7).

Solid-state nuclear magnetic resonance (ssNMR) can provide important structural insights into carbon-based materials. The ^{13}C spectrum is analytically available and is unique to the different structures in

each chemical composition because there is no homocore ^{13}C–^{13}C spin coupling.[39] We used the ssNMR to evaluate the molecular structures of the as-synthesized polymer-like carbon structures, in particular, to identify the formation of different types of ^{13}C bridge-linking structures in the PCN, PCS, and PCF, during the C_{sp2}-C_{sp3} coupling reactions. It is known that NMR is inherently insensitive because of the broad featureless lines caused by multiple anisotropic interactions, and long experiment times caused by inefficient spin-lattice relaxation. Therefore, several ^{13}C solid-state NMR techniques, including single-pulse magic-angle spinning (MAS), cross-polarization MAS (CP-MAS), cross-polarization/total sideband suppression (CP-TOSS), and cross-polarization in combination with polarization inversion (CPPI), were required to obtain information about the bonding motifs and C-C closest neighbor relations (Figure 4). However, solid-state MAS NMR spectra generally remain very broad because of the low resolution caused by the chemical shift anisotropy and inhomogeneous orientation. A cross-polarization (CP) pulse sequence can enhance the sensitivity compared to a simple single-pulse experiment. However, it cannot distinguish between an isotropic peak and a set of spinning sidebands caused by the chemical shift anisotropy at low spinning speeds. The cross-polarization total spinning sideband suppression (CP-TOSS) pulse sequence can suppress the spin sideband, leaving only the isotropic peaks. By using such techniques, ssNMR can distinguish to some extent between different types of carbon, i.e., ^{13}C bridge-linking structures. For example, CPPI can be used to distinguish four types of ^{13}C signals, i.e., nonprotonated quaternary, methine (CH), methylene (CH_2), and methyl (CH_3) carbon resonances.

The 3D PCN-1 (Figures 2A–2i) synthesized by cross-coupling of CH_2Cl_2 and 1,4-dibromobenzene shows two main peaks at δ = 140.75 ppm and 127.96 ppm in the CP-MAS spectrum, which are assigned to sp^2-hybridized aryl carbons coming from phenylene (-C_6H_4-) structure units generated by debromination of 1,4-dibromobenzene in the presence of sodium[40] (Figure 4A). The peaks at 206.96 and 48.47 ppm can be assigned to the set of spinning sidebands of the peak at 127.96 ppm, as demonstrated by the CPMAS-TOSS spectrum, whereas the peak at 40.07 ppm, which appeared in both CP-MAS and CP-MAS-TOSS spectra, is attributed to methylene ($^{13}CH_2$), as demonstrated by the CPPI spectra (Figure 4B and Table S9), because of the appearance of the signal inversion (i.e., negative signals). The peaks at 140.75 ppm and 127.96 ppm of the sp^2-aromatic carbon can be further assigned to quaternary carbon of sp^2-^{13}C(-C) and methine carbon of sp^2-^{13}CH, respectively, as identified by the signal intensity change information; that is, the quaternary aromatic ^{13}C at 140.75 ppm is the least affected and the aromatic ^{13}CH signals at 127.96 ppm can be remarkably suppressed, whereas the remaining $^{13}CH_2$ at 40.07 ppm inverted to negative accompanied by decreasing intensity in the CPPI spectra[41,42] (Figure 4B and Table S9). According to the above information about the bonding motifs and the C-C closest neighbor relationships from the NMR spectra, these three ^{13}C peaks come from the aromatic sp^2C-C and aromatic sp^2 CH, and methylene CH_2, respectively. Therefore, the structural unit in the PCN-1 can be identified as (-H_4C_6-CH_2-C_6H_4-)$_n$ formed by the C(sp^3) (from the CH_2Cl_2 reagent) – C(sp^2) (from the Br-C_6H_4-Br reagent) coupling reactions, and a possible growth route is shown in the supplemental information (Figure S8).

The same procedures were applied to both the 2D PCS-1 (Figures 4C and 4D and Table S10) and the 3D PCF-1 (Figures 4E and 4F and Table S11), respectively, and corresponding growth routes are provided in the supplemental information (Figure S8). For the PCF-1, the peaks at 141.11, and 128.57 ppm shown in CP-MAS can be assigned to aromatic sp^2 carbon, and further assigned to aromatic sp^2C-C and sp^2 CH, respectively, based on the CPPI spectra (Figures 4E and 4F). A very weak peak at 21.55 ppm appears in the single pulse, CP-MAS, and CPMAS-TOSS spectra, and only appears at a contact time of 20 μs in the CPPI spectrum while disappearing at other contact times. This is attributed to the quaternary carbon of the alkyl C-phenyl. Thus, the structure of the PCF-1 is readily understood to be composed of C-(C_6H_4)$_4$ structural units formed by C(sp^3) (from the CBr_4 reagent) – C(sp^2) (from the Br-C_6H_4-Br reagent) coupling reactions (Figures 2C, 4E, 4F, and S8 and Table S11). The 2D sheet-like structure of the PCS-1, which can be observed by TEM (Figure 2B), is formed from C(sp^3) ($CHCl_3$ reagent) – C(sp^2) (Br-C_6H_4-Br reagent) coupling. The peaks in the CPMAS spectrum appeared at 139.35, 128.51 ppm, and 42.08 ppm, whereas spinning sidebands can be observed at 207.93 ppm and 48.71 ppm. However, the spinning sidebands disappeared in the CPMAS-TOSS spectrum (Figure 4C). Based on the CPPI data, we can further assign the peaks at 139.35 and 128.51 ppm to sp^2**C**-C and sp^2**C**H, respectively. It is surprising to observe that the peak appearing at 42.08 ppm is from methylene **C**H_2, which shows negative signals when the contact time changes from 20 to 160 μs in CPPI (Figure 4D). However, no sp^3 CH_2 groups were presenting in this reaction system (Figure 4D and Table S10). This phenomenon may be explained in terms of the following steps: (1) Dehalogenation of $CHCl_3$ and 1,4-dibromobenzene underNa condition will generate $^{\cdot}CHCl_2$, and even all three of the Cl atoms

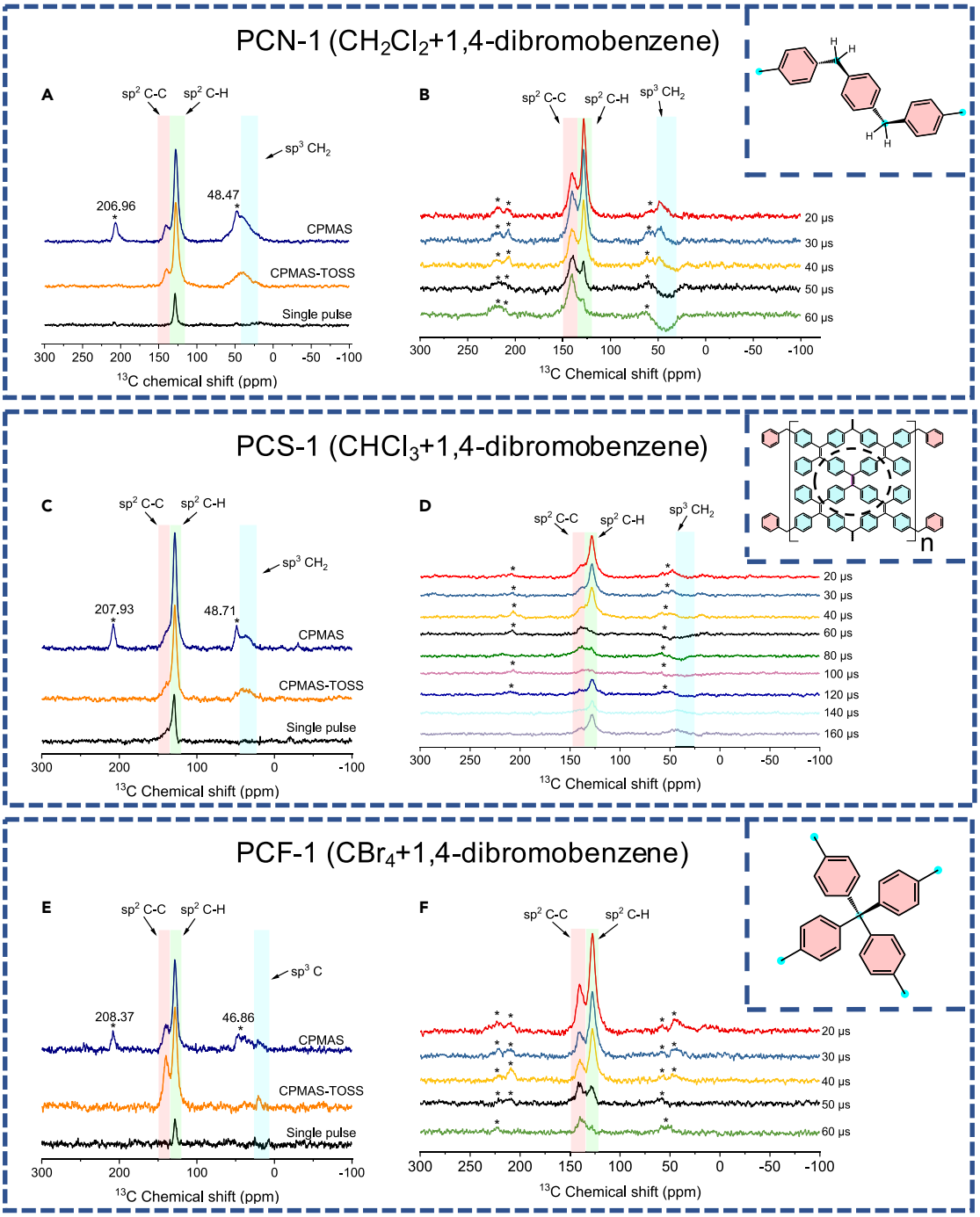

Figure 4. Solid-state magnetic nuclear resonance (ssNMR) spectra of as-synthesized carbon materials

(A and B) for the PCN-1.

(C and D) for the PCS-1.

(E and F) for the PCF-1. (A), (C), and (E) are ^{13}C single-pulse spectra, CP-MAS spectra, and CPMAS-TOSS spectra; (B), (D), and (F) are CPPI spectra.

can be captured by Na, and the 1,4-diradical benzene ($C_6H_4^{\cdot\cdot}$), leading to the radical C(sp^2)-C(sp^3) coupling to generate 1,4-bis(dichloromethyl)benzene (Structure **1**); (2) then, a C(sp^3)-C(sp^3) coupling between two Structure **1** molecules forms *trans-1,2-bis(4-(dichloromethyl)phenyl)ethene* (Structure **2**). This is energetically favorable for removing two neighboring hydrogen atoms (namely, creating an H vacancy pair which

generates holes),[43] because of generating a hydrogen molecule with an energy gain of 0.33 eV,[44] as demonstrated by theoretical calculations for a hydrogenated graphene (i.e., graphene) structure[43,44] (Figure S8B); (3) two molecules of Structure **1** can couple with Structure **2** to form 1,1,2,2-tetraphenylethene (Structure **3**); (4) the growth of the units of Structure **3** after repeating the above-mentioned steps leads to large size nanosheets, which can be terminated by coupling with benzyl radicals after dehydrogenation of the methyl group in toluene to form the PCS-1 nanosheets (Structure **4**).[29,30] This will generate bridged CH_2 groups between the benzene ring and structure **4**. This can account for the existence of the signal from methylene **C**H_2 at 41.9 ppm, which is observed in both the CP-MAS and the CPPI spectra, (Figures 4C and 4D), as well as the sheet morphology (Figures 2B–2i). The possible growth pathways of the as-synthesized highly extended π-conjugated systems, based on the NMR structural information, are illustrated in Figure S8. The sensitivity of ESR is higher than that of ^{1}H NMR because of the electron magnetic moment being much greater than the nuclear magnetic moment. We also know that the detection sensitivity of ^{1}H is 5870 times ^{13}C, because of the natural abundance of ^{13}C being very low, only 1.1%, and the small magnetogyric ratio of ^{13}C.[45] Therefore, the sensitivity of ESR is much larger than that of the ^{13}C NMR. Thus, even if the signal of ^{13}C NMR may not be detected when the population of carbon atoms is below 5%[46] we still can still test the defects signal by ESR, which is a useful complement to the NMR for providing the defect structural information.

Catalytic performance for the selective aerobic oxidation of alcohol-amine cross-coupling over as-synthesized carbon nanostructures

To explore the catalytic performances of the porous carbon nanostructures with high spin densities for direct alcohol imination, we first selected the dehydrogenative coupling reaction between benzyl alcohol and benzylamine as a model system (Detailed experimental procedures are provided in the supplemental information) (Table 1, Figures S9–S41 and Table S12). The catalytic performances of the 3D PCF-1 with a yield of 97.3% (Table 1, entry 17 and Figure S25) and 3D PCN-1 with a yield of 92.0% (Table 1, entry 18 and Figure S26) are lower than that of the 2D-PCS, which has a yield up to 98.0% (Table 1, entry 10 and Figure S18). A variety of factors could influence the superior catalytic performance of 2D PCS-1 compared with the two 3D counterparts. These include: (1) The intrinsic electron transfer rates within the different catalysts; (2) The concentrations of free radical spin defects in the different materials, noting that PCS-1 does not have the highest spin concentration (Table S1); (3) The relative accessibilities of the active catalytic sites in the 2D PCS-1 compared with the 3D counterparts (work on other 2D nanomaterials has indicated that 2D materials are superior in this respect[47]); (iv) the relative concentrations of σ- and π-type radicals in the different materials, because this too can affect the reactivity. In future work, we shall endeavor to quantify the relative contributions of these factors.

Because the catalytic performance of the 2D-PCS material is better than that of the 3D materials, we have focused our detailed catalytic work on the PCS-1. To achieve the best catalytic activity, we varied four parameters[19,48–50]: the reaction atmosphere, temperature, time, and the use of a co-catalyst base (KOH) which has been proven to improve the aerobic oxidative activation of the alcohol.[48]

When the reaction was carried out in a closed-reaction system under air (Table 1, entries 1–3, Figures S9–S11), it showed good catalytic activity with 89% conversion, and selectivity of >99%, and a corresponding yield of 88.1% (Table 1, entry 3 and Figure S11). This indicates that the PCS-1 has potential value as a metal-free catalyst that does not require an inert protective atmosphere.[48,49] Considering the oxidative nature of the imine transformation, we performed the reaction in an oxygen-filled closed-reaction system at room temperatures (25 °C) for further evaluation (Table 1, entry 4 and Figure S12). We were encouraged to find that the PCS-1 has significant activity, even at room temperature, with a conversion of 58.9%, selectivity of the desired imine for >99%, and a corresponding yield of 58.3% (Table 1, entry 4 and Figure S12). We then went on to study the effect of various reaction conditions on the catalytic behavior in the O_2 atmosphere, varying the reaction time, reaction temperature, and whether KOH is used (Table 1, entries 4–10 and Figures S12–S18). These results showed that under optimal catalytic conditions, namely a reaction time of 12 h, a temperature setting at 130 °C, 0.25 mmol of KOH, and in an oxygen atmosphere, the PCS-1 can generate the corresponding imine product with a conversion of >99%, a selectivity of >99%, and a yield of >98.0%, (Table 1, entry 10, and Figure S18). The ^{1}H and ^{13}C NMR spectra and characterization data of the imine (N-benzylidene-1-phenylmethanamine) are given in Figures S29 and S30, respectively. It is surprisingly found, to the best of our knowledge, that the catalytic performance of the PCS-1 is even better than many of the reported metal catalysts, including noble and transition metal complexes.[12,48,49,51] We note that the product is an imine, with water as the only by-product, and that no amines, such as dibenzylamine, can be generated because no H_2 was liberated in the catalytic reaction. It is usually regarded that in

Table 1. Imine synthesis from benzyl alcohol and benzylamine under various reaction conditions

Entry	Catalyst	Condition	Temp. (°C)	Time (h)	KOH (mmol)	Conv. (%)	Sel. (%)	Yield[a] (%)
1	PCS-1	Air	100	12	0.25	77.1	>99	76.3
2	PCS-1	Air	130	12	/	43.2	>99	42.8
3	PCS-1	Air	130	12	0.25	89.0	>99	88.1
4	PCS-1	O_2	25	24	/	58.9	>99	58.3
5	PCS-1	O_2	100	12	/	68.2	>99	67.5
6	PCS-1	O_2	100	12	0.25	94.5	>99	93.6
7	PCS-1	O_2	130	6	/	71.8	>99	71.1
8	PCS-1	O_2	130	6	0.25	97.9	>99	97.0
9	PCS-1	O_2	130	12	/	84.3	>99	83.5
10	PCS-1	O_2	130	12	0.25	>99	>99	>98.0
11	PCS-1 + TEMPO (100 mg)	O_2	130	12	0.25	34.4	36.5	12.6
12	PCS-1 + TEMPO (400 mg)	O_2	130	12	0.25	80.1	–	trace
13	PCS-1 + benzoquinone	O_2	130	12	0.25	51.1	>99	51.1
14[b]	PCS-1	Ar	130	12	0.25	72.2	17.8	12.9
15	PCS-1 + ammonium oxalate (100 mg)	O_2	130	12	0.25	69.5	>99	68.8
16	PCS-1 + ammonium oxalate (400 mg)	O_2	130	12	0.25	40.2	14.7	5.9
17	PCF-1	O_2	130	12	0.25	>99	94.6	93.7
18	PCN-1	O_2	130	12	0.25	>99	92.9	92.0
19	No catalyst	O_2	130	12	/	9.1	73.7	6.7
20	No catalyst	O_2	130	12	0.25	73.6	89.5	65.9

Conditions: benzyl alcohol: 1 mmol, benzylamine: 1 mmol, 2 mL toluene, and 100 mg catalyst.
GC-MS conversion and yield were evaluated using n-Dodecane as the internal standard.
[a]Conversion (%) = 1-n(left alcohol+amine)/n(raw alcohol + amine), Selectivity (%)= n(Imine)/n(products), Yield (%)= Conversion × Selectivity, n represents the number of molars.
[b]The by-product of entry 14 is benzyl benzoate.

the presence of superoxide radicals ($O_2^{\cdot-}$), it reacts with hydrogen to produce water if H_2 is liberated. Metal-free catalytic behavior was confirmed by carrying out inductively coupled plasma mass spectrometry (ICP-MS) (Table S8). Common transition metal impurities, such as Mn, Fe, Co, and Ni, have no effect on the catalytic behavior of the PCS-1, because their levels are lower than those of previously reported "metal-free" catalysts, such as Mn < 15 ppm,[52] Fe < 300 ppm,[53] Co < 5 ppm,[54] Ni < 10 ppm.[19] For comparison, the levels in our PCS-1 catalyst are Mn ~2 ppm, Fe 66 ppm, Co 0.15 ppm, Ni ~1 ppm (Table S8).

In addition to yield, conversion rate, and selectivity, another key challenge for developing metal-free catalysts is recyclability. So far, some carbon-based metal-free catalysts have shown poor reusability because of the loss of their active sites or deactivation after catalytic reactions.[17] However, the PCS-1 can be easily recovered and reused, and does not lose catalytic efficiency even after 10 cycle tests (Figures S31–S41 and Table S12), which greatly improves the economic efficiency. Based on the results of ESR measurements (Figure 3E and Table S1), we postulate that the key factor determining the excellent catalytic efficiency of the PCS-1 is its carbon nanostructure which has a high electron spin density and holes generated by removing two neighboring hydrogen atoms (namely, H vacancy pairs), as mentioned above. To further understand the oxidative alcohol-amine cross-coupling mechanism, we first conducted active species trapping experiments to clarify the contribution of the different intermediates to the reaction. Compared to the optimal conditions (Table 1, entry 10), other experimental parameters were unchanged except for adding 100 mg (Table 1, entry 11) or 400 mg (Table 1, entry 12) of 2,2,6,6-tetramethylpiperidine-1-oxyl (TEMPO) as a radical trapping agent for the PCS-1. The corresponding catalytic results showed that the selectivity drastically decreased to 36.5% and the yield was suppressed to 12.6% (Table 1, entry 11 and Figure S19), or the yield was close to zero, although with a conversion of 80.1% (Table 1, entry 12 and Figure S20). These results demonstrate that the high radical spin concentration of the PCS-1 is a very important factor in the high efficiency of our carbon-catalyzed imine process, which is favorable for forming a high concentration of superoxide radicals ($O_2^{\cdot-}$).

To verify the function of superoxide radicals in our aerobic reactions,[17] we added benzoquinone as an $O_2^{\cdot-}$ scavenger.[37] The results show that the benzyl alcohol underwent no conversion in the absence of $O_2^{\cdot-}$, whereas the self-coupling of benzylamine to generate imine can be observed, with a conversion of only 51.1% accompanied by a yield of 51.1% (Table 1, entry 13 and Figure S21). Alternatively, when carrying out the reaction under an argon atmosphere, it was found that the conversion to imine was 72.2, % with a selectivity of 17.8% and a low yield of 12.9% (Table 1, entry 14 and Figure S22), whereas for the self-coupling of alcohol to form benzyl benzoate,[55] the selectivity was found to be 82.2%, resulting in a yield of 59.3% (Table 1, entry $14^{(4)}$ and Figure S22). Based on the above results, we can therefore confirm that the superoxide radical is the major reactive species for the oxidative alcohol substrate. To assess the function of holes in the aerobic reaction, we added 1 or 4 equiv of ammonium oxalate as a hole scavenger,[37] whereupon the reaction decreased from the conversion of 69.5% with a yield of 68.8% to a conversion of 40.2% and a yield of 5.9%, respectively (Table 1, entries 15 & 16 and Figures S23 and S24). This is attributed to the holes being scavenged by ammonium oxalate. Based on the blank control experimental results (Table 1, entries 19 & 20 and Figures S27 and S28), we can further demonstrate the reliability of the above conclusions, i.e., superoxide radicals and holes synergistically make a major contribution to the high catalytic performance of the PCS-1 in our imine synthesis.

Inspired by the excellent activity of the PCS-1 in the aerobic oxidation of benzyl alcohol and benzylamine cross-coupling reaction, we proceeded to examine an asymmetric imine transformation by taking aniline and benzyl alcohol as catalytic substrates. This produced a conversion of >99% and selectivity of >99% for benzylidene aniline with a yield of >98% for asymmetric imine transformation (Figure S42), which demonstrates the universality of the PCS-1 as an imine transformation catalyst (Figure 1). In comparison, the corresponding yields of the other two catalysts, i.e., the PCN-1 and the PCF-1 were 92% and 93.7%, respectively (Table S13).

Probing the underlying mechanism of the direct alcohol imination reaction

The porous structure of the 2D PCS-1 provides a high surface area for heterogeneous catalysis and good accessibility to the catalytically active sites for the vapor phase reactant (O_2) and liquid phase reactants (benzyl alcohol and amines, including benzylamine or aniline).[38,55] It is known that molecular oxygen (O_2) is easily reduced to the superoxide radical anion ($O_2^{\cdot-}$) because of the high electronegativity of the oxygen atom.[56] Thus, the adsorbed O_2 can be reduced to $O_2^{\cdot-}$ by unpaired electrons from the PCS-1, which serves to leave the holes free to react.[57] Thermal excitation to generate e-h pairs does not require any other type of initiation, which can be caused by defects.[58] Note that the positive "hole" is created in the valence band (VB) whereas an electron is transferred to the conduction band (CB) after thermal excitation.[58] By performing calculations aimed at comparing the defect state with the defect-free state, we found that the energy level of the conduction band (CB or the lowest unoccupied molecular orbital, LUMO) downshifted from −1.2027 eV in the defect-free state to −1.9987 eV in a defect state, whereas the energy level of the valence band (VB, or highest occupied molecular orbital, HOMO) changed from −5.3187 eV in the defect-free state to −6.2812 eV in the defect state, thus leading to a band-gap (E_g) reduction from 4.1160 in the defect-free state to 3.3445 eV in the defect state (Figures 5A and 5B). This makes it easier to generate electron-hole pairs by thermal excitation for the PCS-1, thus making the PCS-1 an appropriate catalyst for catalytic oxidation.[13] Furthermore, the electron spin density has an asymmetric distribution, as shown in Figure 5B-ii, which indicates that the PCS-1 defect states with unpaired electrons are spin polarized. The charge density of the PCS-1 is synergistically altered by unpaired electrons (Figure 5B-iii and Table S14), which is believed to play an important role in the electron-donating process for imine transformation.[59] Primary benzylamine is firmly anchored to the catalytic system to form an electron-donor complex that is subsequently oxidized to form the radical cation by the positive charge of the hole.[57] We, therefore, carried out first-principles density functional theory (DFT) calculations on the reaction pathway free-energy profiles for further validation of the reaction mechanism hypothesis (Figure 5C).

The initial species (hole in VB and electron in CB) can either react directly with the organic reagents when adsorbed on the surface of the particle, or they may be converted into reactive intermediates which react with the organic pollutants either directly on the surface or close to it.[57] Therefore, the benzyl alcohol undergoes complete oxidation under the influence of $O_2^{\cdot-}$, transforms to an aldehyde (TS1),[59] and then reacts with the benzylamine radical complex (TS2) to generate N-benzylidene-1-phenylmethanamine. It then passes through different transition states (TS3-5) to finally form the corresponding imine and amide, whereas this process appears to be concomitant with the elimination of one molecule of water in the case of pathways 2 and 3,[17,48] pathway 1 to generate amide is less kinetic favorable. Assuming hydrogen generation happens, it will immediately react

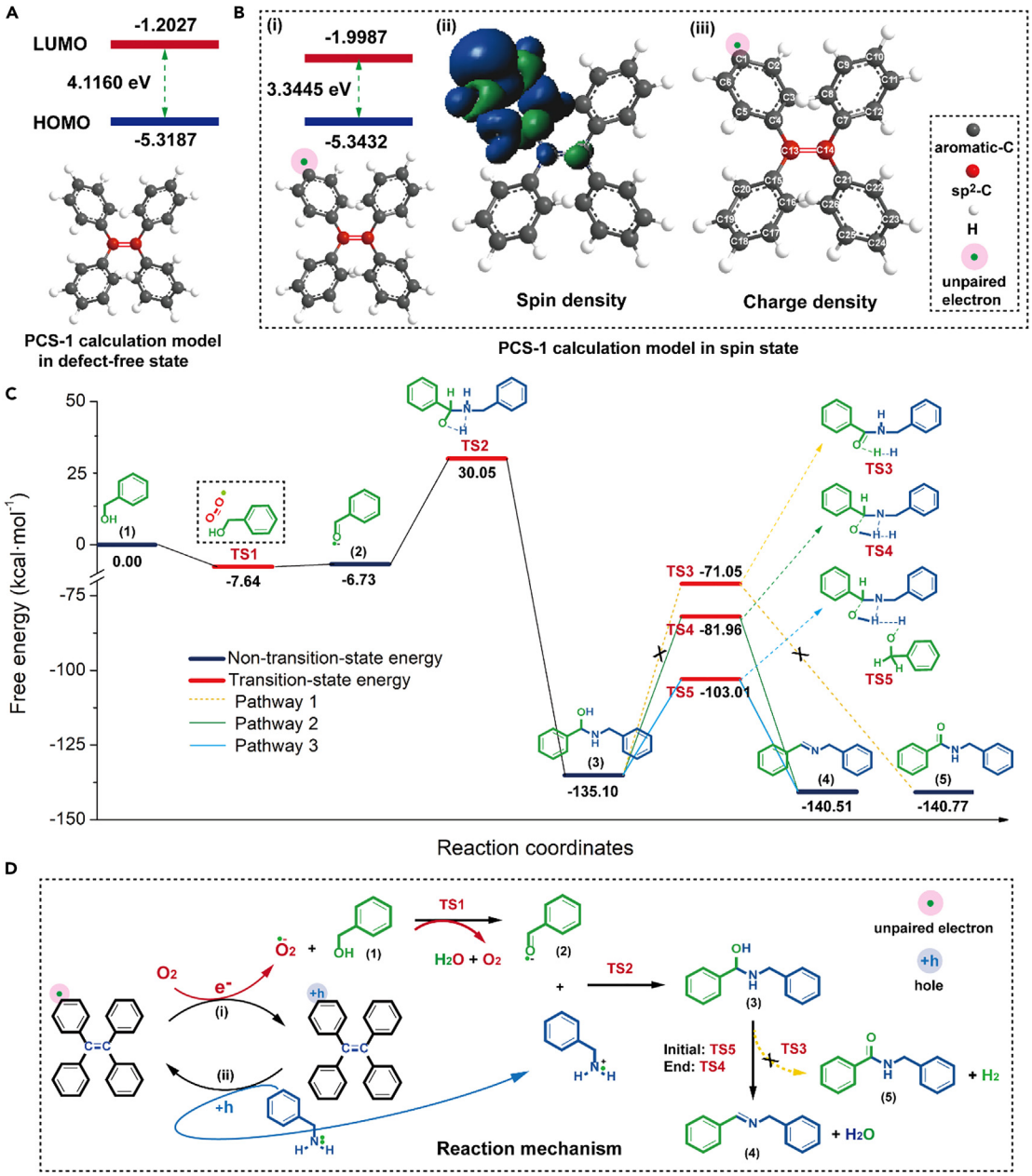

Figure 5. High spin catalyzed dehydrogenative coupling of alcohols and amines analysis

(A) Theoretical calculations of the HOMO and LUMO distributions of PCS-1 in a defect-free state.

(B) HOMO and LUMO, spin density distribution and charge density distributions of PCS-1 with an unpaired electron.

(C) Thermodynamic and kinetic calculations of the reaction pathway free-energy profile calculated for the formation of N-benzylidene-1-phenylmethanamine.

(D) Schematic representation of the electron transfer and summarized reaction mechanism.

with oxygen to generate water, which prevents the hydrogen from reducing imines to produce amines.[12] Meanwhile, the active site is released for another catalytic cycle, giving rise to a turnover mechanism. Based on the above analysis, a plausible mechanism for imine synthesis is proposed (Figure 5D). The proposed catalytic mechanism is attributed to high concentrations of unpaired electrons in the carbon nanostructures, which reduce oxygen to form the superoxide radical anion ($O_2^{\cdot -}$). This can react with alcohol to form an anion radical, followed by a positively charged hole reacting with the amine to form a radical cation. At the same time, the active site is released for another catalytic cycle whereas the anion radical reacts with a cation radical to form the imine.

The coexistence of the characteristic signals of superoxide and benzylamine radical combinations was confirmed by using 5,5-dimethyl-1-pyrroline N-oxide (DMPO) as a spin-trapping agent in ESR measurements under environmental conditions of 25 and 130°C, respectively.[60,61] This provided us not only with clear evidence of the proposed reaction mechanism for a spin-induced, electron transfer catalytic coupling reaction, but also with the reason behind the faster reaction rate, higher conversion, and larger yields at the higher temperature of 130 °C (compared to 25 °C) because of the higher concentrations of intermediate radicals generated under these conditions (Figure S43).

Conclusions

In this work, we have developed a C(sp^2)-C(sp^3) free radical coupling reaction for constructing carbon nanostructures with different dimensionalities (both 2D and 3D) and high spin densities. Among these, the 2D PCS-1 exhibits impressive catalytic behavior for alcohol imination with excellent cycle performance and high catalytic efficiency, as compared with the current noble/transition metal complexes. This approach to carbon-catalyzed organic imine synthesis opens up a promising new route for organic synthesis.

Limitations of the study

Although the key role of electron spin in the catalytic performance of carbon catalysts has been highlighted, this study does not include a detailed relationship between the spin components of the carbon catalysts and catalytic behavior. Moreover, in future studies, a more detailed structural analysis of carbon catalysts should be performed by EELS, neutron diffraction, etc.

STAR★METHODS

Detailed methods are provided in the online version of this paper and include the following:

- KEY RESOURCES TABLE
- RESOURCE AVAILABILITY
  - Lead contact
  - Materials availability
  - Data and code availability
- EXPERIMENTAL MODEL AND SUBJECT DETAILS
- METHOD DETAILS
  - Synthesis of PCF
  - Synthesis of PCS
  - Synthesis of PCN
  - Physical structure characterizations
  - Catalytic performances tests

SUPPLEMENTAL INFORMATION

Supplemental information can be found online at https://doi.org/10.1016/j.isci.2023.106659.

ACKNOWLEDGMENTS

This work was financially supported by the National Natural Science Foundation of China (No. 22171158), the Engineering Research Center of Advanced Rare Earth Materials, (Ministry of Education, China), Department of Chemistry, Tsinghua University (Beijing 100084, China), and the Tribology Science Fund of State Key Laboratory of Tribology (SKL TKF20B18). The GC-MS test was provided by Prof. Chanjuan Xi, Prof. Yongge Wei, and Prof. Chao Chen. the Tsinghua Xuetang Talents Program for providing computational resources and VASP software copyright funds. Variable temperature ESR measurements were performed on the Steady High Magnetic Field Facilities, High Magnetic Field Laboratory, Chinese Academy of Sciences (CAS). XANES measurements were performed on the 4B9B beamline at the Beijing Synchrotron Radiation Facility, Chinese Academy of Sciences (CAS).

AUTHOR CONTRIBUTIONS

H.C. and A.K.C. led and designed the project. C.W., Z.Q., and Y.T. performed the synthesis and characterization. Z.Q., Y.T., and H.Y. carried out ssNMR tests. H.C., C.W., Z.Q., Y.T., and A.K.C. jointly analyzed and discussed all data and co-wrote the manuscript.

DECLARATION OF INTERESTS

The authors declare that they have no competing interests.

Received: October 11, 2022
Revised: January 13, 2023
Accepted: April 7, 2023
Published: April 10, 2023

REFERENCES

1. Sprung, M.A. (1940). A summary of the reactions of aldehydes with amines. Chem. Rev. *26*, 297–338. https://doi.org/10.1021/cr60085a001.

2. He, R., Jin, X., Chen, H., Huang, Z.-T., Zheng, Q.-Y., and Wang, C. (2014). Mn-catalyzed three-component reactions of imines/nitriles, Grignard reagents, and tetrahydrofuran: an expedient access to 1,5-amino/keto alcohols. J. Am. Chem. Soc. *136*, 6558–6561. https://doi.org/10.1021/ja503520t.

3. Kobayashi, S., Mori, Y., Fossey, J.S., and Salter, M.M. (2011). Catalytic enantioselective formation of C-C bonds by addition to imines and hydrazones: a ten-year update. Chem. Rev. *111*, 2626–2704. https://doi.org/10.1021/cr100204f.

4. Khan, A.M., Abid, O.U.R., and Mir, S. (2020). Assessment of biological activities of chitosan Schiff base tagged with medicinal plants. Biopolymers *111*, e23338. https://doi.org/10.1002/bip.23338.

5. Wilson, M.R., Solà, J., Carlone, A., Goldup, S.M., Lebrasseur, N., and Leigh, D.A. (2016). An autonomous chemically fueled small-molecule motor. Nature *534*, 235–240. https://doi.org/10.1038/nature18013.

6. Stoddart, J.F. (2017). Mechanically interlocked molecules (MIMs)-molecular shuttles, switches, and machines. Angew. Chem. Int. Ed. *56*, 11094–11125. https://doi.org/10.1002/anie.201703216.

7. Wu, Y., Hu, L., Li, Z., and Deng, L. (2015). Catalytic asymmetric umpolung reactions of imines. Nature *523*, 445–450. https://doi.org/10.1038/nature14617.

8. Belowich, M.E., and Stoddart, J.F. (2012). Dynamic imine chemistry. Chem. Soc. Rev. *41*, 2003–2024. https://doi.org/10.1039/C2CS15305J.

9. Chen, H., Yan, L., and Wei, H. (2018). Mechanism of boron-catalyzed N-alkylation of primary and secondary arylamines with ketones using silanes under "wet" conditions. Organometallics *37*, 3698–3707. https://doi.org/10.1021/acs.organomet.8b00405.

10. Chu, G., and Li, C. (2010). Convenient and clean synthesis of imines from primary benzylamines. Org. Biomol. Chem. *8*, 4716–4719. https://doi.org/10.1039/C0OB00043D.

11. Jiang, G., Chen, J., Huang, J.-S., and Che, C.-M. (2009). Highly efficient oxidation of amines to imines by singlet oxygen and its application in Ugi-type reactions. Org. Lett. *11*, 4568–4571. https://doi.org/10.1021/ol9018166.

12. Gnanaprakasam, B., Zhang, J., and Milstein, D. (2010). Direct synthesis of imines from alcohols and amines with liberation of H_2. Angew. Chem. Int. Ed. *49*, 1468–1471. https://doi.org/10.1002/ange.200907018.

13. Li, X.-H., and Antonietti, M. (2013). Polycondensation of boron- and nitrogen-codoped holey graphene monoliths from molecules: carbocatalysts for selective oxidation. Angew. Chem. Int. Ed. *52*, 4572–4576. https://doi.org/10.1002/anie.201209320.

14. Largeron, M., and Fleury, M.-B. (2013). Bioinspired oxidation catalysis. Science *339*, 43–44. https://doi.org/10.1126/science.1232220.

15. Nakamura, E., and Sato, K. (2011). Managing the scarcity of chemical elements. Nat. Mater. *10*, 158–161. https://doi.org/10.1038/nmat2969.

16. Silverio, D.L., Torker, S., Pilyugina, T., Vieira, E.M., Snapper, M.L., Haeffner, F., and Hoveyda, A.H. (2013). Simple organic molecules as catalysts for enantioselective synthesis of amines and alcohols. Nature *494*, 216–221. https://doi.org/10.1038/nature11844.

17. Abednatanzi, S., Gohari Derakhshandeh, P., Leus, K., Vrielinck, H., Callens, F., Schmidt, J., Savateev, A., and Van Der Voort, P. (2020). Metal-free activation of molecular oxygen by covalent triazine frameworks for selective aerobic oxidation. Sci. Adv. *6*, eaaz2310. https://doi.org/10.1126/sciadv.aaz2310.

18. Jie, X., Shang, Y., Chen, Z.-N., Zhang, X., Zhuang, W., and Su, W. (2018). Differentiation between enamines and tautomerizable imines in the oxidation reaction with TEMPO. Nat. Commun. *9*, 5002. https://doi.org/10.1038/s41467-018-07534-x.

19. Yang, H., Cui, X., Dai, X., Deng, Y., and Shi, F. (2015). Carbon-catalysed reductive hydrogen atom transfer. Nat. Commun. *6*, 6478. https://doi.org/10.1038/ncomms7478.

20. Zhang, Y., Pang, S., Wei, Z., Jiao, H., Dai, X., Wang, H., and Shi, F. (2018). Synthesis of a molecularly defined single-active site heterogeneous catalyst for selective oxidation of N-heterocycles. Nat. Commun. *9*, 1465. https://doi.org/10.1038/s41467-018-03834-4.

21. Step, E.N., Buchachenko, A.L., and Turro, N.J. (1994). Paramagnetic interactions of triplet radical pairs with nitroxide radicals: an "Antiscavenging" effect. J. Am. Chem. Soc. *116*, 5462–5466. https://doi.org/10.1021/ja00091a059.

22. Buchachenko, A.L., and Berdinsky, V.L. (2002). Electron spin catalysis. Chem. Rev. *102*, 603–612. https://doi.org/10.1021/cr010370l.

23. Buchachenko, A.L., and Berdinsky, V.L. (2004). Spin catalysis as a new type of catalysis in chemistry. Russ. Chem. Rev. *73*, 1033–1039. https://doi.org/10.1070/RC2004v073n11ABEH000888.

24. Khavryuchenko, O.V., and Peslherbe, G.H. (2016). Spin catalysis over conductive solids: enhancing the rate of model C-C bond cracking over carbon nanoparticles. ChemCatChem *8*, 3156–3160. https://doi.org/10.1002/cctc.201600723.

25. Morita, Y., and Nishida, S. (2010). Phenalenyls, cyclopentadienyls, and other carbon-centered radicals. In Stable radicals: fundamentals and applied aspects of odd-electron Compounds, R.G. Hicks, ed. (Wiley). https://doi.org/10.1002/9780470666975.ch3.

26. Li, Y., Jia, Z., Xiao, S., Liu, H., and Li, Y. (2016). A method for controlling the synthesis of stable twisted two-dimensional conjugated molecules. Nat. Commun. *7*, 11637. https://doi.org/10.1038/ncomms11637.

27. Rugg, B.K., Phelan, B.T., Horwitz, N.E., Young, R.M., Krzyaniak, M.D., Ratner, M.A., and Wasielewski, M.R. (2017). Spin-selective photoreduction of a stable radical within a covalent donor-acceptor-radical triad. J. Am. Chem. Soc. *139*, 15660–15663. https://doi.org/10.1021/jacs.7b10458.

28. Arifullin, M.R., and Berdinskii, V.L. (2013). Spin states of multielectron systems and the action of multi-spin bans. Russ. J. Phys. Chem. *87*, 1186–1190. https://doi.org/10.1134/S0036024413070042.

29. Cao, H., Wang, C., Li, B., Chen, T., Han, P., Zhang, Y., Yang, H., Li, Q., and Cheetham, A.K. (2022). Successive free-radical C (sp^2)–C (sp^2) coupling reactions to form graphene. CCS Chem. *4*, 584–597. https://doi.org/10.31635/ccschem.021.202100919.

30. Tian, Y., Cao, H., Yang, H., Yao, W., Wang, J., Qiao, Z., and Cheetham, A.K. (2023). Electron spin catalysis with graphene belts. Angew. Chem. Int. Ed. *62*, e202215295. https://doi.org/10.1002/anie.202215295.

31. Panickar, R., Sobhan, C.B., and Chakravorti, S. (2020). Chemical vapor deposition synthesis of carbon spheres: effects of temperature and

hydrogen. Vacuum *172*, 109108. https://doi.org/10.1016/j.vacuum.2019.109108.

32. Ferrari, A.C., and Robertson, J. (2000). Interpretation of Raman spectra of disordered and amorphous carbon. Phys. Rev. B *61*, 14095–14107. https://doi.org/10.1103/PhysRevB.61.14095.

33. Williams, D.H., and Fleming, I. (2008). Spectroscopic Methods in Organic Chemistry (McGraw-Hill Higher Education). https://doi.org/10.1007/978-3-030-18252-6.

34. Cataldo, F., Putz, M.V., Ursini, O., Angelini, G., Garcia-Hernandez, D.A., and Manchado, A. (2016). A new route to graphene starting from heavily ozonized fullerenes: Part 3 an electron spin resonance study. Fuller. Nanotub. Car. N. *24*, 195–201. https://doi.org/10.1080/1536383X.2015.1113524.

35. Ye, J., Ni, K., Liu, J., Chen, G., Ikram, M., and Zhu, Y. (2017). Oxygen-rich carbon quantum dots as catalysts for selective oxidation of amines and alcohols. ChemCatChem *10*, 259–265. https://doi.org/10.1002/cctc.201701148[.

36. Dias, J.R. (2008). On the spectacular structural isomorphism between C_nH_s monoradical and $C_{n+s}H_{S+3}$ diradical benzenoid hydrocarbons: from reactive intermediates to vacancy (hole) defects in graphite. J. Phys. Chem. A *112*, 3260–3274. https://doi.org/10.1021/jp7114077.

37. Xiao, Y., Tian, G., Li, W., Xie, Y., Jiang, B., Tian, C., Zhao, D., and Fu, H. (2019). Molecule self-assembly synthesis of porous few-layer carbon nitride for highly efficient photoredox catalysis. J. Am. Chem. Soc. *141*, 2508–2515. https://doi.org/10.1021/jacs.8b12428.

38. M. Beller, A. Renken, and A. van Santen, eds. (2012). Catalysis: from principles to applications (Wiley-VCH).

39. Sathyanarayana, D.N. (2013). Introduction to Magnetic Resonance Spectroscopy ESR, NMR NQR, Second Edition (I K International Publishing House).

40. Zhuo, S., Shi, Y., Liu, L., Li, R., Shi, L., Anjum, D.H., Han, Y., and Wang, P. (2018). Dual-template engineering of triple-layered nanoarray electrode of metal chalcogenides sandwiched with hydrogen-substituted graphdiyne. Nat. Commun. *9*, 3132. https://doi.org/10.1038/s41467-018-05474-0.

41. Wu, X.L., and Zilm, K.W. (1993). Complete spectral editing in CPMAS NMR. J. Magn. Reson. *102*, 205–213. https://doi.org/10.1006/jmra.1993.1092.

42. Wu, X.L., Burns, S.T., and Zilm, K.W. (1994). Spectral editing in CPMAS NMR. Generating subspectra based on proton multiplicities. J. Magn. Reson. *111*, 29–36. https://doi.org/10.1006/jmra.1994.1222.

43. Gao, H., Wang, L., Zhao, J., Ding, F., and Lu, J. (2011). Band gap tuning of hydrogenated graphene: H coverage and configuration dependence. J. Phys. Chem. C *115*, 3236–3242. https://doi.org/10.1021/jp1094454.

44. Tsetseris, L., and Pantelides, S.T. (2012). Hydrogen uptake by graphene and nucleation of graphane. J. Mater. Sci. *47*, 7571–7579. https://doi.org/10.1007/s10853-012-6447-6.

45. Silverstein, R.M., Webster, F.X., Kiemle, D.J., and Bryce, D.L. (2015). Spectrometric Identification of Organic Compounds, 8th Edition (Wiley-VCH).

46. Navalon, S., Dhakshinamoorthy, A., Alvaro, M., and Garcia, H. (2014). Carbocatalysis by graphene-based materials. Chem. Rev. *114*, 6179–6212. https://doi.org/10.1021/cr4007347.

47. Shifa, T.A., Wang, F., Liu, Y., and He, J. (2019). Heterostructures based on 2D materials: a versatile platform for efficient catalysis. Adv. Mater. *31*, 1804828. https://doi.org/10.1002/adma.201804828.

48. Gunanathan, C., and Milstein, D. (2013). Applications of acceptorless dehydrogenation and related transformations in chemical synthesis. Science *341*, 1229712. https://doi.org/10.1126/science.1229712.

49. Mukherjee, A., Nerush, A., Leitus, G., Shimon, L.J.W., Ben David, Y., Espinosa Jalapa, N.A., and Milstein, D. (2016). Manganese-catalyzed environmentally benign dehydrogenative coupling of alcohols and amines to form aldimines and H_2: a catalytic and mechanistic study. J. Am. Chem. Soc. *138*, 4298–4301. https://doi.org/10.1021/jacs.5b13519.

50. Daw, P., Kumar, A., Espinosa-Jalapa, N.A., Ben-David, Y., and Milstein, D. (2019). Direct synthesis of amides by acceptorless dehydrogenative coupling of benzyl alcohols and ammonia catalyzed by a manganese pincer complex: unexpected crucial role of base. J. Am. Chem. Soc. *141*, 12202–12206. https://doi.org/10.1021/jacs.9b05261[.

51. Mon, M., Adam, R., Ferrando−Soria, J., Corma, A., Armentano, D., Pardo, E., and Leyva−Pérez, A. (2018). Stabilized Ru $[(H_2O)_6]^{3+}$ in confined spaces (MOFs and zeolites) catalyzes the imination of primary alcohols under atmospheric conditions with wide scope. ACS Catal. *8*, 10401–10406. https://doi.org/10.1021/acscatal.8b03228.

52. Wang, Y., Shen, Y., Zhou, Y., Xue, Z., Xi, Z., and Zhu, S. (2018). Heteroatom-doped graphene for efficient NO decomposition by metal-free catalysis. ACS Appl. Mater. Interfaces *10*, 36202–36210. https://doi.org/10.1021/acsami.8b09503.

53. Murata, T., Kotsuki, K., Murayama, H., Tsuji, R., and Morita, Y. (2019). Metal-free electrocatalysts for oxygen reduction reaction based on trioxotriangulene. Commun. Chem. *2*, 46. https://doi.org/10.1038/s42004-019-0149-9.

54. Xiong, W., Wang, Z., He, S., Hao, F., Yang, Y., Lv, Y., Zhang, W., Liu, P., and Luo, H. (2020). Nitrogen-doped carbon nanotubes as a highly active metal-free catalyst for nitrobenzene hydrogenation. Appl. Catal., B *260*, 118105. https://doi.org/10.1016/j.apcatb.2019.118105.

55. Su, C., Acik, M., Takai, K., Lu, J., Hao, S.-J., Zheng, Y., Wu, P., Bao, Q., Enoki, T., Chabal, Y.J., and Loh, K.P. (2012). Probing the catalytic activity of porous graphene oxide and the origin of this behaviour. Nat. Commun. *3*, 1298. https://doi.org/10.1038/ncomms2315.

56. Togo, H. (2004). Advanced Free Radical Reactions for Organic Synthesis (Elsevier).

57. Rhodes, C.J. (2014). Unpaired electrons as probes of catalytic systems. Sci. Prog. *97*, 303–370. https://doi.org/10.3184/003685014X14151169734173.

58. Streetman, B.G., and Banerjee, S.K. (2016). Solid State Electronic Devices, Seventh Edition (Pearson Education Limited).

59. Luo, J., Yu, H., Wang, H., Wang, H., and Peng, F. (2014). Aerobic oxidation of benzyl alcohol to benzaldehyde catalyzed by carbon nanotubes without any promoter. Chem. Eng. J. *240*, 434–442. https://doi.org/10.1016/j.cej.2013.11.093.

60. Chernick, E.T., Casillas, R., Zirzlmeier, J., Gardner, D.M., Gruber, M., Kropp, H., Meyer, K., Wasielewski, M.R., Guldi, D.M., and Tykwinski, R.R. (2015). Pentacene appended to a TEMPO stable free radical: the effect of magnetic exchange coupling on photoexcited pentacene. J. Am. Chem. Soc. *137*, 857–863. https://doi.org/10.1021/ja510958k.

61. Ke, J., Tang, Y., Yi, H., Li, Y., Cheng, Y., Liu, C., and Lei, A. (2015). Copper-catalyzed radical/radical C_{sp3}-H/P-H cross-coupling: -phosphorylation of aryl ketone O-acetyloximes. Angew. Chem. Int. Ed. *54*, 6604–6607. https://doi.org/10.1002/ange.201501287.

STAR★METHODS

KEY RESOURCES TABLE

REAGENT or RESOURCE	SOURCE	IDENTIFIER
Chemicals, peptides, and recombinant proteins		
Carbon tetrabromide (CTB)	Tokyo Chemical Industry (Shanghai)	CAS Number: 558-13-4
Chloroform (TCM)	Beijing Tongguang fine chemicals company	CAS Number: 67-66-3
Dichloromethane (DCM)	Beijing Tongguang fine chemicals company	CAS Number: 75-09-2
1,4-Dibromobenzene (1,4-DBB)	Meryer Shanghai	CAS Number: 106-37-6
4,4-Dibromobiphenyl (4,4-DBBP)	Meryer Shanghai	CAS Number: 92-86-4
1,3,5-Tribromobenzene (1,3,5-TBB)	Meryer Shanghai	CAS Number: 626-39-1
Metal Sodium	Thermo Fisher Acros Organics	CAS Number: 7440-23-5
Toluene	Beijing Chemical Works	CAS Number: 108-88-3
Software and algorithms		
OriginPro 2022b	Origin Lab	https://www.originlab.com/
Chemdraw 21.0.0	PerkinElmer	https://www.perkinelmer.com/category/chemdraw
Other		
TEM	Hitachi	Hitachi H7650B
ESR	Bruker	EMXplus Spectrometer
GC-MS	Shimadzu	QP 2010 Plus
ssNMR	JEOL	JNM-ECZ600R
Heating ESR	JEOL	FA-200

RESOURCE AVAILABILITY

Lead contact

Further information and requests should be directed to and will be fulfilled by the lead contact, Huaqiang Cao (hqcao@mail.tsinghua.edu.cn)

Materials availability

This study did not generate new unique reagents

Data and code availability

- All data reported in this paper will be shared by the lead contact upon request.
- This study does not generate any original code.
- Any additional information required to reanalyzed the data reported in this paper is available from the lead contact upon request.

EXPERIMENTAL MODEL AND SUBJECT DETAILS

This work does not use any experimental models.

METHOD DETAILS

Synthesis of PCF

In a typical synthesis procedure, 60.0 mg of CTB and 85.4 mg of 1,4-DBB were dissolved in 40 mL of dehydrated toluene (The toluene was pre-dehydration treated by small amounts of metal sodium for about 3 h and remained in the supernatant) with stirring to form a homogeneous solution in a Teflon-lined stainless steel autoclave of 50 mL capacity, followed by rapidly adding 200 mg of metal sodium in small pieces into the above autoclave with stirring. Then the mixture was sealed and maintained at 180 °C for 50 h. After the

autoclave was cooled down to ambient temperature naturally, the products were collected and washed with absolute alcohol and deionized water for depleting the incomplete reaction of sodium metal and various residues. The as-obtained PCF-1 solid product was then vacuum dried at 60 °C for 24 h. Further, it underwent annealing treatment under inert Argon gas at different annealing temperatures of 450 °C for 3h. Replaced the 1,4-DBB to 4,4-DBBP (112.9 mg) or 1,3,5-TBB (76.0 mg), respectively, at the same mole ratio to react with CTB and followed the same reaction procedure, we could eventually get the PCF-2 and PCF-3.

Synthesis of PCS

In a typical synthesis procedure, 130 μL of TCM and 85.4 mg of 1,4-DBB were dissolved in 40 mL of dehydrated toluene (The toluene was pre-dehydration treated by small amounts of metal sodium for about 3 h and remained the supernatant) with stirring to form a homogeneous solution in a Teflon-lined stainless steel autoclave of 50 mL capacity, followed by rapidly adding 200 mg of metal sodium in small pieces into the above autoclave with stirring. Then the mixture was sealed and maintained at 180 °C for 50 h. After the autoclave was cooled down to ambient temperature naturally, the products were collected and washed with absolute alcohol and deionized water for depleting the incomplete reaction of sodium metal and various residues. The first deionized water-rinsed supernatant was collected for 72 h dialysis to eventually obtain stable and homogeneous PCS-1 suspensions. The as-obtained PCS-1 solid product was then vacuum dried at 60 °C for 24h. Further, it underwent annealing treatment under inert Argon gas at a different annealing temperature of 450 °C for 3h. Replaced the 1,4-DBB to 4,4-DBBP (112.9 mg) or 1,3,5-TBB (76.0 mg), respectively, at the same mole ratio to react with TCM and followed the same reaction procedure, we could eventually get the PCS-2 and PCS-3.

Synthesis of PCN

In a typical synthesis procedure, 24 μL of DCM and 85.4 mg of 1,4-DBB were dissolved in 40 mL of dehydrated toluene (The toluene was pre-dehydration treated by small amounts of metal sodium for about 3 h and remained the supernatant) with stirring to form a homogeneous solution in a Teflon-lined stainless steel autoclave of 50 mL capacity, followed by rapidly adding 200 mg of metal sodium in small pieces into the above autoclave with stirring. Then the mixture was sealed and maintained at 180 °C for 50 h. After the autoclave was cooled down to ambient temperature naturally, the products were collected and washed with absolute alcohol and deionized water for depleting the incomplete reaction of sodium metal and various residues. The as-obtained PCN-1 solid product was then vacuum dried at 60 °C for 24 h. Further, it underwent annealing treatment under inert Argon gas at a different annealing temperature of 450 °C for 3h. Replaced the 1,4-DBB to 4,4-DBBP (112.9 mg) or 1,3,5-TBB (76.0 mg), respectively, at the same mole ratio to react with DCM and followed the same reaction procedure, we could eventually get the PCN-2 and PCN-3.

Physical structure characterizations

The morphology images of PCS and PCN were captured by TEM (Hitachi H7650B), under different magnifications with an accelerating voltage of 80 kV. XRD (Bruker D8 ADVANCE X-ray powder diffractometer, Germany) measurements were carried out for the phase structure characterization. It was occupied with Cu Kα radiation (λ = 1.5406 Å, 40 kV, 40 mA), at the scanning rate of 0.01 S^{-1} with 2θ ranging from 5° to 80°.Raman spectra were recorded for phase structure characterization by a LabRAM HR Evolution Raman spectrometer (HORIBA Jobin Yvon, France) with laser wavelength at 532 nm of 5% power under ambient temperature. The structure of as-synthesized carbon catalysts was detected by FTIR (Perkin Elmer Spectrum 100), in the measuring range of 450–4000 cm^{-1}. The electron spin density of samples was calculated by solid-state ESR spectra test with a conventional CW X-band (ν = 9–9.8 GHz) spectrometer (Bruker EMXplus Spectrometer System, Germany) equipped with an Oxford ESR 910 helium continuous-cryostat with 100 kHz magnetic field modulation. $CuSO_4 \cdot 5H_2O$ (99.99%, Shanghai Aladdin Biochemical Technology Co., Ltd) was used as a spin standard substance for spin density quantitative calculation. Samples were sealed in capillaries, respectively. Typically, different microwave power and frequencies were 0.1 mW and 9.405323 GHz for the as-synthesized sample powder, and 2.0 mW and 9.406612 GHz for $CuSO_4 \cdot 5H_2O$, respectively. The Programmable Goniometer was applied for acquiring spectra at different orientations of the applied magnetic field concerning the samples. The spectra were also corrected taking into account the variation of the quality factor of the resonators with temperature. The solid samples were annealed in a tube furnace at 450 °C for 3 h under an argon atmosphere, respectively, followed by cooling down to room temperature naturally. The Brunauere-Emmett-Teller (BET) specific surface areas,

and the Barrett-Joyner-Halenda (BJH) pore volume and size distribution were obtained from the N2 adsorption-desorption isotherms recorded at 77 K on a BET Quantachrome Autosorb (IQ Station 2, USA). All measurements were performed using the above samples after pre-treatment at 300 °C for outgas procedure under vacuum conditions. Different carbon types can be analyzed by ^{13}C solid-state Nuclear Magnetic Resonance (^{13}C ssNMR). The spectra were recorded by the JEOL JNM-ECZ600R 600 MHz NMR spectrometer equipped with a 3.2 mm tube diameter double-resonance probe with a dipolar decoupling method at room temperature. The main magnetic field strength was 14.1 T (T), and the corresponding ^{1}H and ^{13}C Larmor frequencies were 600 MHz and 150. 91 MHz, respectively. The ^{13}C chemical shifts were referenced directly to adamantine as the external reference material at 29.47 ppm for higher accuracy. All the spectra were recorded at 12 kHz MAS. Single pulse spectra were obtained with direct ^{13}C excitation by a $\pi/2$ pulse with 2.5 μs width, 1200 scans and 3 s relaxation delay. CPMAS spectra were obtained with a $\pi/2$ pulse with 2.5 μs width for ^{1}H excitation and 2 ms contact time, 1200 scans and 3 s relaxation delay. CPMAS-TOSS spectra were obtained by the CPMAS followed by a group of TOSS sequences for the suppression of spinning sidebands, 1200 scans and 3 s relaxation delay. CPPI spectra were obtained by the CPMAS followed by a group of PI sequences with an inversion time from 20 μs to 160 μs, 1200 scans and a 3 s relaxation delay for every single spectrum. The elemental analysis (EA) test for the content of carbon and hydrogen was conducted by Element Analyzer (Vario EL III). The decomposition temperature was set as 950–1200°C, while the separation device was an adsorption/desorption column and equipped with TCD thermal conductivity detector. The test method was to test the content of carbon and hydrogen elements in the "CHN" mode. XANES data were tested on the 4B9B beamline at the Beijing Synchrotron Radiation Facility, Chinese Academy of Sciences (CAS). The powder sample was first uniformly adhered to a conductive tape and attached to a specific substrate. Then C K-edge XANES measurements in transmission mode were performed under ambient conditions, with an X-ray beam incident at an angle of 50° to the sample surface. Samples after the catalytic performance were first washed with absolute alcohol and ethyl acetate to remove the organic residual. Then they were digested with a moderate amount of Nitric Acid (65–70% in content, 99.9999% in purity, ThermoFisher). For better accuracy of measurement, the background signal was deducted during the process and the Standard Curve Method was carried out. The solution sample was loaded into the Inductively Coupled Plasma-Mass Spectrometry (ICP-MS, iCAP Q, ThermoFisher, USA) in the characterization mode of KED for the element content detection of Mn, Fe, Co, Ni.

Catalytic performances tests

The catalytic experiment for N-benzylidene-1-phenylmethanamine synthesis. A 25-mL Schlenk tube was firstly charged with the as-synthesized PCS-1 catalyst (100 mg), KOH (14 mg, 0.25 mmol), and toluene (2 mL). Then, equimolar amounts of benzyl alcohol (1 mmol) and benzylamine (1 mmol) were weighed for preparation. Solid materials were transferred into the Schlenk tube under air, the Schlenk tube was subsequently connected to a Schlenk line and vacuum-oxygen exchange was done three times. Liquid compounds and solvents were charged under an oxygen flow. The Schlenk tube was then placed into an oil bath and heated to a given temperature and stirred for a given time. Upon the reaction was finished, the reaction mixture was cooled to room temperature. Then ethyl acetate was added into the mix and centrifuged for the separation of liquid product and solid catalyst. In this way, the PCS-1 catalyst can be reused for multi-runs by simple filtration and rinsing in deionized water, anhydrous ethanol, and acetone, respectively. Also, the PCF-1 and PCN-1 were applied to the catalysis, respectively, and obeyed the same procedures. Based on the above experimental procedures, add TEMPO (100 mg), *p*-benzoquinone (100 mg), and ammonium oxalate (100 mg) respectively into the reaction system as blank control experiments while keeping other operation processes consistent, or carry out the reaction under argon atmosphere to test the aerobic oxidation activity. After the post-treatment, the product was dispersed in 8 mL ethyl acetate. Added a moderate amount of product solution into the GC-MS bottle and diluted it to 2 mL with ethyl acetate for the characterization preparation. Then the conversion and yield of N-benzylidene-1-phenylmethanamine were evaluated using n-Dodecane as the internal standard and were determined based on area normalization by GC-MS (Shimadzu-QP 2010 Plus). As for the reaction system preparation, a moderate amount of PCS-1 was added to the mixture of 1 mmol of benzylamine and 1 mmol of benzyl alcohol in 2 mL of toluene. The reaction mixture was vigorously stirred at ambient conditions a bubbled with oxygen for 0.5 h. Then 500 μL of this reaction solution was taken out with the addition of 5 μL of DMPO, then used a capillary tube was to absorb the appropriate amount and loaded into a quartz paramagnetic tube. The reaction system was analyzed by ESR under an O_2 atmosphere at 25 °C and 130 °C, respectively. The typical test parameters were set as Microwave power: 20 mW.

Microwave Frequency: 9.4 GHz. Scan time: 2 min. Modulation amplitude: 0.02 mT. Modulation Frequency: 100 kHz. Receiver gain: 102. The time constant: is 0.01. After the reaction, the catalyst was washed with deionized water, anhydrous ethanol, and acetone, respectively, separated by centrifugation and dried for use in subsequent applications. The catalyst exhibited stability for at least ten runs without any deactivation.